Hindawi Publishing Corporation
International Journal of Navigation and Observation
Volume 2008, Article ID 325279, 12 pages
doi:10.1155/2008/325279

Research Article

CLEAN Technique for Polarimetric ISAR

M. Martorella,[1] A. Cacciamano,[1] E. Giusti,[1] F. Berizzi,[1] B. Haywood,[2] and B. Bates[2,3]

[1] *Department of Information Engineering, University of Pisa, via Caruso 16, 56122 Pisa, Italy*
[2] *Defence Science & Technology Organisation, Edinburgh, SA 5111, Australia*
[3] *School of Electrical & Electronic Engineering, University of Adelaide, SA 5005, Adelaide, Australia*

Correspondence should be addressed to A. Cacciamano, andrea.cacciamano@iet.unipi.it

Received 19 February 2008; Accepted 3 June 2008

Recommended by M. Greco

Inverse synthetic aperture radar (ISAR) images are often used for classifying and recognising targets. To reduce the amount of data processed by the classifier, scattering centres are extracted from the ISAR image and used for classifying and recognising targets. This paper addresses the problem of estimating the position and the scattering vector of target scattering centres from polarimetric ISAR images. The proposed technique is obtained by extending the CLEAN technique, which was introduced in radar imaging for extracting scattering centres from single-polarisation ISAR images. The effectiveness of the proposed algorithm, namely, the Polarimetric CLEAN (Pol-CLEAN) is tested on simulated and real data.

1. INTRODUCTION

The CLEAN algorithm was introduced in radio astronomy to reduce sidelobe-induced artefacts. In [1], the authors use the CLEAN technique to alleviate two types of artefacts introduced by the point spread function (PSF) sidelobes in real aperture radar images. Such a technique iteratively estimates the PSF of the brightest scatterer and removes it from the formed image.The CLEAN technique was applied later to inverse synthetic aperture radar (ISAR) imaging with interesting results [2]. Recently, fully polarimetric radars have been largely used for synthetic aperture radar (SAR) application [3, 4] as well as, although less extensively, for ISAR applications [5]. The advantage of fully polarimetric data is due to the fact that scattering mechanisms and target properties can be identified by measuring scattering matrices [6–9]. Inverse synthetic aperture radar (ISAR) images prove useful when used for classifying and recognising targets [10, 11]. Nevertheless, the image data size is often too large to implement real time classifiers. For this reason, algorithms such as the CLEAN technique can be employed for reducing the data size significantly without losing useful information. The problem of reducing the amount of data without losing useful information is even more critical when dealing with polarimetric ISAR images, since the data size is three to four times larger. An algorithm for scattering centre extraction from polarimetric SAR (PolSAR) images was proposed in [12]. In [12], the signal model was strongly based on the SAR geometry, which is known a priori. In the ISAR case, the non-cooperativity of the target does not allow using any such knowledge. So a parametric model is introduced to account for unknown target motions. Therefore, the problem of estimating the model parameters and the scattering centre extraction problem must be solved jointly. Moreover, in typical ISAR scenarios, only the received radar echo is presumed to be available (no ancillary data is used). In this paper, a polarimetric CLEAN (Pol-CLEAN) technique is proposed by extending the CLEAN technique in [2] in order to extract target features such as the position of the scattering centres and their scattering matrix. It is worth pointing out that the novelty of the proposed Pol-CLEAN technique, with respect to the CLEAN technique, lies on the extension to polarimetric ISAR images and on a new method for estimating the scattering centre point spread function.

The signal model is introduced in Section 2 whereas the Pol-CLEAN technique is detailed in Section 3. The effectiveness of the proposed algorithm is tested on simulated and real data and presented in Section 4.

2. SIGNAL MODEL

The polarimetric matrix of the received signal, in free space conditions, can be written in a time-frequency domain by

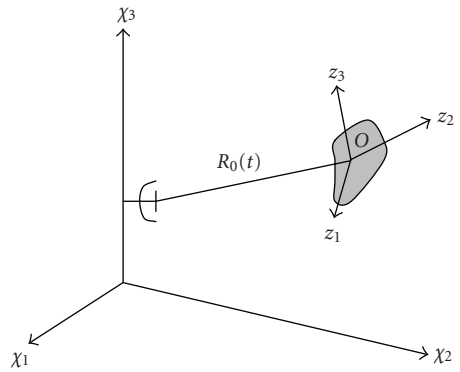

Figure 1: Radar-target geometry.

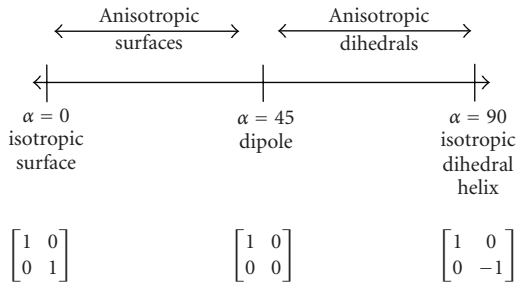

Figure 2: Interpretation of the internal degree of freedom α.

extending the signal model defined in [13]

$$\mathbf{S}_R(f,t) = W(f,t)\exp\left[-j\frac{4\pi f}{c}R_0(t)\right] \cdot \int_V \boldsymbol{\zeta}(\mathbf{z})\exp\left\{-j\frac{4\pi f}{c}\left[\mathbf{z}^T\cdot\mathbf{i}_{R_0}^{(\mathbf{z})}(t)\right]\right\}d\mathbf{z} + \mathbf{N}(f,t), \quad (1)$$

where $\mathbf{S}_R(f,t) = \begin{bmatrix} S_R^{HH}(f,t) & S_R^{HV}(f,t) \\ S_R^{VH}(f,t) & S_R^{VV}(f,t) \end{bmatrix}$ is expressed by means of a polarimetric matrix, $W(f,t) = \text{rect}[t/T_{\text{obs}}]\text{rect}[(f-f_0)/B]$ represents a rectangular window in the time-frequency domain (t,f), f_0 is the carrier frequency, B is the transmitted signal bandwidth, T_{obs} is the observation time, V is the spatial domain where the scattering matrix $\boldsymbol{\zeta}(\mathbf{z}) = \begin{bmatrix} \zeta^{HH}(\mathbf{z}) & \zeta^{HV}(\mathbf{z}) \\ \zeta^{VH}(\mathbf{z}) & \zeta^{VV}(\mathbf{z}) \end{bmatrix}$ is defined, and $\mathbf{N}(f,t) = \begin{bmatrix} N^{HH}(f,t) & N^{HV}(f,t) \\ N^{VH}(f,t) & N^{VV}(f,t) \end{bmatrix}$ is the polarimetric matrix containing the noise. With reference to Figure 1, $\mathbf{z}$ is the vector that locates a generic scatterer, $R_0(t)$ is the modulus of vector $\mathbf{R}_0(t)$, which locates the focusing point O and $\mathbf{i}_{R_0}^{(z)}(t)$ the unit vector of $\mathbf{R}_0(t)$. The function rect(x) is equal to 1 for $|x| < 0.5$, 0 otherwise.

Before proceeding, it is convenient to use a different notation, as detailed in [7], and exploit the characteristic of isotropic media that are encountered in ISAR applications. Therefore, the polarimetric data that represents the received signal can be written according to Pauli's decomposition as follows:

$$\mathbf{S}_R = \frac{1}{\sqrt{2}}\left[S_R^{VV} + S_R^{HH}, S_R^{VV} - S_R^{HH}, 2S_R^{HV}\right]^T = A\mathbf{k}, \quad (2)$$

where $A = |\mathbf{k}|$ and where the dependence on (f,t) is omitted for notation simplicity. The polarimetric unit vector $\mathbf{k}$ is defined as follows:

$$\mathbf{k} = \left[\cos\alpha e^{j\delta}, \sin\alpha\cos\beta e^{j\gamma}, \sin\alpha\sin\beta e^{j\varphi}\right], \quad (3)$$

where β represents the physical rotation of the scatterer about the radar line of sight (LoS), δ, γ, and φ are the scatterer phases in the three polarimetric channels, and α is a scatterer internal degree of freedom, which ranges in the interval $[0°, 90°]$. It must be pointed out that the angle α is rotation invariant and therefore it is decoupled from β. An interpretation of the internal degree of freedom α is given in Figure 2.

It is worth noting that such a representation is meant to highlight the physical properties of the scattering mechanism induced by a given scatterer. Therefore, by defining the unit vector $\mathbf{k}$, it is possible to define a specific polarisation that resonates with a scatterer with given physical properties. It must also be pointed out that the same decomposition applies for the target scattering matrix. Therefore, the scattering vector obtained from the scattering matrix is $\boldsymbol{\zeta}(\mathbf{z}) = [\zeta^{VV}(\mathbf{z}) + \zeta^{HH}(\mathbf{z}), \zeta^{VV}(\mathbf{z}) - \zeta^{HH}(\mathbf{z}), 2\zeta^{HV}(\mathbf{z})]$.

2.1. Signal separation

The Range-Doppler technique is based on an approximation that allows considering a rectangular support for the received signal in the Fourier domain. Such an approximation also leads to the separation of the domain in two independent one-dimensional domains: a time and a frequency component. Therefore, the received signal, relative to a single point-like scatterer, can be written in terms of the product of a time and a frequency component as follows:

$$s_R^{(i)}(t,f) = s_1^{(i)}(t)s_2^{(i)}(f), \quad (4)$$

where

$$s_1^{(i)}(t) = B_i\exp\left(j2\pi\left(\eta + f_d t + \frac{\mu}{2}t^2\right)\right)\text{rect}\left(\frac{t}{T_{\text{ob}}}\right), \quad (5)$$

$$s_2^{(i)}(f) = A_i\exp\left(j2\pi f\tau_0\right)\text{rect}\left(\frac{f-f_o}{B}\right), \quad (6)$$

where the product A_iB_i represents the complex amplitude in the ith Pauli channel, f_d is the Doppler frequency, μ is the chirp rate, and τ_0 is the time delay associated with the scattering centre. It is worth pointing out that the parameter μ is related to the signal model, which accounts for a quadratic radial motion, that is, it includes Doppler acceleration. Therefore, it should not be confused with the transmitted signal chirp rate if any is employed.

3. POL-CLEAN

The Pol-CLEAN technique is derived from the CLEAN technique proposed in [2]. Specifically, the Pol-CLEAN works iteratively by

(1) locating the brightest scattering centre in the polarimetric ISAR image and therefore by finding its coordinates in the delay-Doppler image plane (τ^*, ν^*),

(2) extracting its polarimetric vector $\mathbf{k}_s$, and

(3) removing it from the ISAR image in order to extract the next brightest scattering centre.

In order to eliminate a scattering centre from an ISAR image, the scattering centre point spread function (PSF) must be estimated and subtracted from the ISAR image. Let $S^{(1)}(f,t)$, $S^{(2)}(f,t)$ and $S^{(3)}(f,t)$ be the received signal in the three Pauli channels. After motion compensation, three ISAR images, namely, $I^{(1)}(\tau,\nu)$, $I^{(2)}(\tau,\nu)$ and $I^{(3)}(\tau,\nu)$ are obtained by means of a 2D Fourier Transform. The brightest scattering centre (dominant scatterer) is found within the three images. The range and cross-range indexes τ^* and ν^* and the Pauli's channel i^*, which corresponds to the polarimetric channel that contains the brightest scattering centre, are extracted by means of (7)

$$(\tau^*,\nu^*,i^*) = \arg\max_{(\tau,\nu,i)}\{\,|I^{(i)}(\tau,\nu)|\,\}, \tag{7}$$

with $i \in \{1,2,3\}$, $\tau \in \{1,2,\ldots,M\}$, $\nu \in \{1,2,\ldots,N\}$ and where M and N are the number of range and cross-range bins. The estimation of the PSF is performed by minimising the image energy after scattering centre removal. In order to find an efficient solution of the nonlinear optimisation problem stated in (7), the received signal separation is exploited.

3.1. Time component

By referring to (5), B_i ($i \in \{1,2,3\}$), f_d, and μ are the parameters to be estimated. The constant η can be neglected, because it does not affect the shape of the PSF. The signal $s_1^{(i)}(t)$, which is an N-dimensional row vector, is Fourier transformed to obtain a cross-range profile. A cost function is defined by means of the energy remaining in the range bin after scattering centre deletion. In order to treat the optimisation problem in a real domain, the scattering centre deletion is performed by considering the absolute value of the range profile. Such an operation can be performed in a single channel and then applied to the remaining channels by adjusting the corresponding B_i parameter. It must be pointed out that only the magnitude $\widetilde{B}$ of B must be estimated at this stage whereas the phase component is estimated separately and directly from the image. In summary, the following optimisation problem can be stated:

$$\left\{\hat{f}_d,\hat{\mu},\widehat{\widetilde{B}}_{i^*}\right\} = \arg\min_{(f_d,\mu,\widetilde{B}_{i^*})}\{E_{d_{i^*}}(f_d,\mu,\widetilde{B}_{i^*})\}, \tag{8}$$

where $E_{d_{i^*}} = \int |d_{i^*}(\nu)|^2 d\nu$ is the energy of a Doppler section in the i^*th Pauli channel, with $d_{i^*}(\nu) = |I^{(i^*)}(\tau^*,\nu)| - |S_1^{(i^*)}(\nu)|$ and $S_1^{(i^*)}(\nu)$ the Fourier Transform of $s_1^{(i^*)}(t)$. The estimates $\hat{f}_d$ and $\hat{\mu}$ are then used in the remaining Pauli channels for estimating the complex amplitudes B_i (with $i \neq i^*$). The latter estimation problem is transformed into an optimisation problem as follows:

$$\left\{\widehat{\widetilde{B}}_i\right\} = \arg\min_{\widetilde{B}_i}\{E_{d_i}(\hat{f}_d,\hat{\mu},\widetilde{B}_i) \text{ with } i \neq i^*\}, \tag{9}$$

where $E_{d_i} = \int |d_i(\nu)|^2 d\nu$ is the energy of a Doppler section in the ith Pauli channel ($i \neq i^*$) with $d_i(\nu) = |I^{(i)}(\tau^*,\nu)| - |S_1^{(i)}(\nu)|$.

3.2. Frequency component

A similar procedure is followed to estimate the frequency component of the PSF. The signal component in (6) is an M-dimensional column vector. After selecting a Doppler bin and range compressing via the Fourier Transform, a section of the ith channel ISAR image $I^{(i)}(\tau,\nu^*)$ can be obtained. Then, the delay τ_0 is jointly estimated with the magnitude $\widetilde{A}_{i^*}$ (in the i^*th Pauli channel) as follows:

$$\{\hat{\tau}_0,\widehat{\widetilde{A}}_{i^*}\} = \arg\min_{(\tau_0,\widetilde{A}_{i^*})}\{E_{g_{i^*}}(\tau_0,\widetilde{A}_{i^*})\}, \tag{10}$$

where $E_{g_{i^*}} = \int |d_{g_{i^*}}(\nu)|^2 d\nu$ is the energy of a delay section in the i^*th Pauli channel, with $g_{i^*}(\nu) = |I^{(i^*)}(\tau,\nu^*)| - |S_2^{(i^*)}(\tau)|$ and $S_2^{(i^*)}(\tau)$ the inverse fourier transform of $s_2^{(i^*)}(f)$.

The remaining two complex amplitudes are separately estimated by solving two separate one-dimensional optimisation problems:

$$\widetilde{A}_i = \arg\min_{\widetilde{A}_i}\{E_{g_i}(\hat{\tau}_0,\widetilde{A}_i)\} \quad \text{with } i \neq i^*, \tag{11}$$

where $E_{g_i} = \int |d_{g_i}(\nu)|^2 d\nu$ is the energy of a delay section in the ith Pauli channel ($i \neq i^*$) with $g_i(\nu) = |I^{(i)}(\tau,\nu^*)| - |S_2^{(i)}(\tau)|$.

3.3. Scattering centre PSF

The scattering centre PSF in the ith Pauli channel is obtained by calculating the two dimensional Fourier Transform of the product of the time and frequency components multiplied by the phase extracted from the ISAR image, as analytically detailed in

$$I_{\mathrm{PSF}}^{(i)}(\tau,\nu) = \left|\mathrm{FT}^2\left\{\hat{s}_1^{(i)}(t)\hat{s}_2^{(i)}(f)\right\}\right| \cdot \angle(I^{(i)}(\tau,\nu)). \tag{12}$$

The scattering vector $\mathbf{k}_s(\tau^*,\nu^*)$ relative to the considered scattering centre is therefore available by calculating the three scattering centre PSF centred in (τ^*,ν^*). Then, at the generic kth iteration, the scattering centre must be eliminated from the ISAR image via (13) in order to extract the following brightest scatterer:

$$I_{k+1}^{(i)}(\tau,\nu) = I_k^{(i)}(\tau,\nu) - I_{\mathrm{PSF}_k}^{(i)}(\tau,\nu). \tag{13}$$

The algorithm stops when the energy of the signal component in the ISAR image at the kth iteration is lower than a given threshold, λ. Such a threshold is typically set to 5% of the initial energy, that is, the total energy of the polarimetric ISAR image before any component removal. In mathematical detail, the preset threshold depends on the energy content and on the SNR of the initial ISAR image, as detailed in (14)

$$\lambda = K \cdot E\frac{\mathrm{SNR}}{\mathrm{SNR}+1}, \tag{14}$$

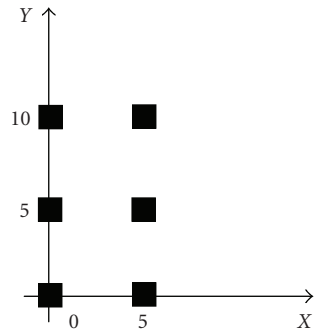

Figure 3: Six-point target geometry.

where $E^{(\mathbf{I}(\tau,\nu))} = \sum_{i=1}^{3} E^{(I^{(i)}(\tau,\nu))}$, with $E^{(I^{(i)}(\tau,\nu))} = \iint |I^{(i)}(\tau, \nu)|^2 d\tau\, d\nu$. It is worth pointing out that a coefficient SNR/(SNR + 1) is used in order to account for the energy of the signal component (noiseless image). Moreover, the SNR can be estimated in the image domain by selecting image areas where no target is present. It must also be noted that the energy of the signal component of the ISAR image at each iteration has to be compared to the energy threshold in (14). Therefore, the iterations stop when $E_k^{(\mathbf{I}(\tau,\nu))}(\text{SNR}/(\text{SNR} + 1)) < \lambda$.

4. RESULTS

The algorithm performance is tested both by using simulated and real data. The simulation test highlights the algorithm effectiveness when extracting ideal point-like scatterers, whereas the real data test shows an example of the output when the Pol-CLEAN is applied to "real-world" data.

4.1. Simulation

The analysis of simulated data aims at testing the Pol-CLEAN effectiveness when the target is composed of a number of ideal point-like scatterers with different polarimetric properties. Two separate tests are run. The first concerns a six-point target with scatterers placed at a distance of 5 resolution cells from each other. The second experiment is proposed to test the Pol-CLEAN robustness when the point-like scatterers distance drops down to one resolution cell.

4.1.1. Six-point target

An X-band radar and a six-point target are considered for the generation of the received signal. Each point is located at a distance of 5 resolution cells from the others (as shown in Figure 3). The scattering matrices relative to each point are shown in Table 1, whereas the main radar parameters are shown in Table 2.

The simulation is repeated by changing the zero padding in order to test the algorithm robustness with respect to the image oversampling. Specifically, zero padding factor (ZPF) of 1, 2, 4, and 8 are considered (note that ZPF = 1 means "no zero padding"). Gaussian noise has been added to the raw data in order to have an SNR = −10 dB (in the data domain).

Table 1: Scattering centre characteristics.

Type	Scattering matrix
S_1 Surface ($\alpha = 0°$)	$\begin{bmatrix} 1 & 0 \\ 0 & 1 \end{bmatrix}$
S_2 Dihedral ($\alpha = 90°, \beta = 0°$)	$\begin{bmatrix} 1 & 0 \\ 0 & -1 \end{bmatrix}$
S_3 Dipole ($\alpha = 45°, \beta = 45°$)	$\begin{bmatrix} 1+\frac{\sqrt{2}}{2} & \frac{\sqrt{2}}{2} \\ \frac{\sqrt{2}}{2} & 1-\frac{\sqrt{2}}{2} \end{bmatrix}$
S_4 Dihedral ($\alpha = 90°, \beta = 30°$)	$\begin{bmatrix} \frac{\sqrt{3}}{2} & \frac{1}{2} \\ \frac{1}{2} & -\sqrt{\frac{3}{2}} \end{bmatrix}$
S_5 Surface ($\alpha = 0°$)	$\begin{bmatrix} 1 & 0 \\ 0 & 1 \end{bmatrix}$
S_6 Dipole ($\alpha = 45°, \beta = 60°$)	$\begin{bmatrix} \frac{3}{2} & \frac{\sqrt{3}}{2} \\ \frac{\sqrt{3}}{2} & \frac{1}{2} \end{bmatrix}$

The estimated scattering vectors are decomposed according to (2) and (3) (only parameters α and β are shown). The estimated type of scattering (α) matches the true values as well as the estimated orientation angle (β), as shown in Table 3, where the mean value of the couple of parameters (α, β), obtained by generating 25 noise realisations, is shown. It is worth noting that the estimated mean values are weakly affected by the ZPF whereas the standard deviation decreases when the zero padding increases, as shown in Figure 4, where the root mean square error (RMSE) of α and β is plotted as a function of the ZPF.

The original ISAR images and the ISAR images after the first and the last scattering centre elimination are shown in Figures 5, 6, and 7 for the three Pauli channels, respectively. All ISAR images are obtained by using ZPF = 8. It is worth noting that the first component removal only affects the first Pauli channel (HH+VV) since the extracted scatterer has zero-components in the other two Pauli channels (VV-HH and 2HV) It can be pointed out that, after the last elimination, the scatterer's contribution is significantly suppressed.

4.1.2. Robustness analysis with respect to scatterer's distance

An algorithm performance loss is expected when the distance between the scatterers reduces. With the present experiment,

Table 2: Radar parameters.

Central freq. (f_0)	10 GHz	No. of radar sweeps (N)	96
Bandwidth (B)	400 MHz	Cross-range res.	0.68 m
Freq. step (Δf)	3.15 MHz	Range res.	0.375 m
No. of tx freq. (M)	128	SNR (data domain)	−10 dB

Table 3: Estimated scattering parameters.

ZP		S_1	S_2	S_3	S_4	S_5	S_6
1	α	55.5°	85.99°	45.53°	86.73°	6.55°	45.40°
	β	—	0.07°	45.12°	29.88°	—	61.39°
2	α	5.02°	86.64°	45.43°	86.91°	5.64°	45.08°
	β	—	0.23°	45.16°	29.51°	—	61.44°
4	α	5.06°	86.56°	45.20°	86.74°	5.52°	45.22°
	β	—	−0.13°	45.13°	29.47°	—	61.52°
8	α	4.97°	86.71°	45.37°	86.96°	5.44°	45.15°
	β	—	−0.09°	45.19°	29.71°	—	61.43°

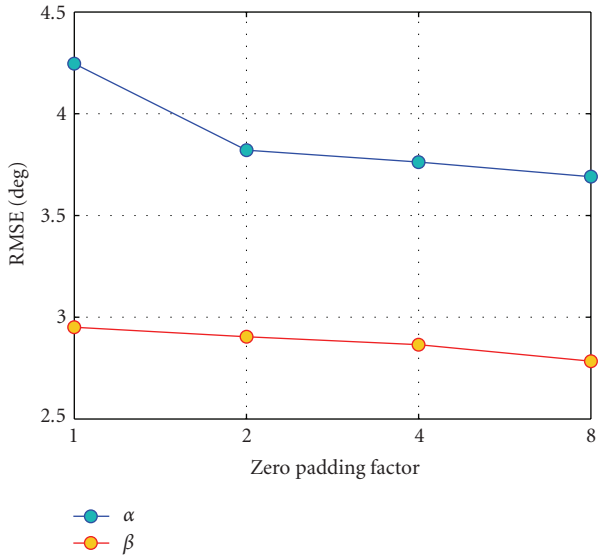

Figure 4: Standard deviation versus zero padding factor.

the algorithm robustness with respect to the interference caused by the vicinity of other scatterers is tested. Specifically, two scatterers close to each other are considered in order to create such an interference. The scatterers chosen are $S1$ and $S4$ (from the previous experiment) and their scattering matrices are shown in Table 1. Gaussian noise is added to the generated data in order to obtain a SNR = −10 dB (in the data domain). Both the vicinity along the range and cross-range coordinate is tested. In particular, the scatterer's distance is varied within one to five range cells, first along the range direction and then along the cross-range direction. Figure 8 shows the results in terms of estimation error for the parameters α and β against the distance in range (as in the number of range resolution cells), whereas Figure 9 shows the similar results against the distance in cross-range (as in number of cross-range resolution cells). The results are shown in terms of the RMSE and they are obtained by using a ZPF = 8.

As predicted, the performance of the algorithm decreases when the distance between scatterers reduces. It can also be pointed out that the same conclusions are reached when considering range and cross-range directions. This effect is mainly due to two reasons.

(1) Scatterers interfere with each other because of their sidelobes. Although it would be tempting to use a window in order to reduce the sidelobe level, the inconvenient effect of widening the main lobe would negatively affect the performance when the distance is equal to one resolution cell.

(2) The cancellation of the scatterer under test is a non-linear operation that affects the estimated scattering matrix of the nearest scatterers.

4.2. Real data

The analysis of real data provides a clear example of the results achievable when using the Pol-CLEAN. Since no accurate target model is available, a direct error analysis is not viable for this kind of experiment. Nevertheless, the results are visually readable by comparing the extracted scatterers with the Pol-ISAR image.

4.2.1. Data set description

The data used for this test is collected during a real turn-table experiment. The data is obtained from the GTRI publicly releasable data set. The experiment is run by using a stepped-frequency fully polarimetric radar system arranged on a tower and looking down to a turn-table. The illuminated target is a T72 tank. The data file contains 79 radar sweeps for a fixed elevation angle (θ_{el} = 29.9994°). After each radar sweep, the turn table is rotated by 0.05°. Therefore, a total azimuth angle variation of 3.9° is spanned about

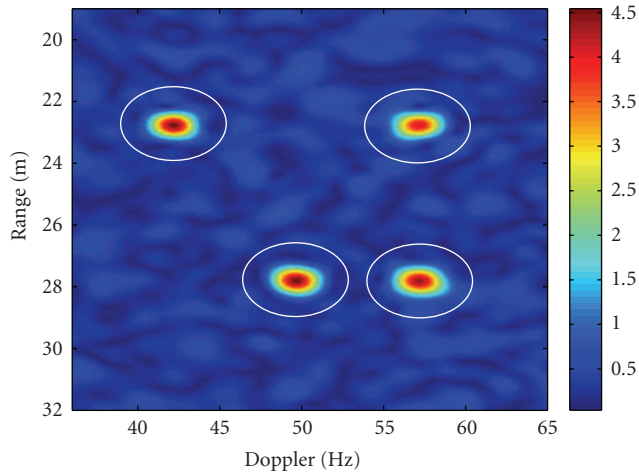

(a)

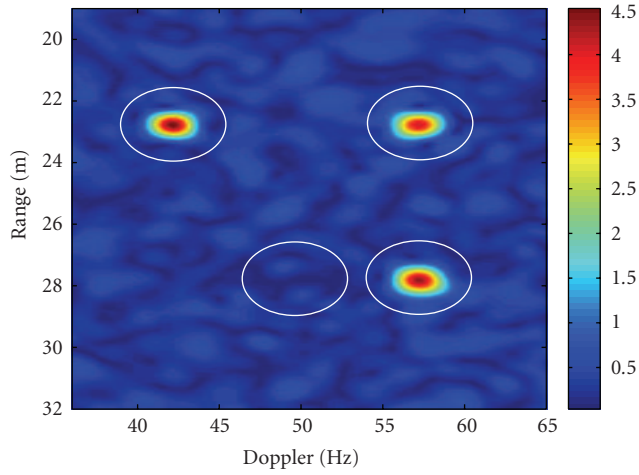

(b)

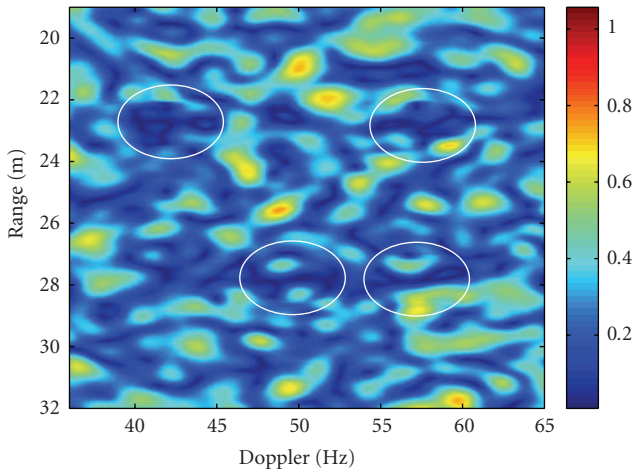

(c)

Figure 5: ISAR image on channel HH+VV before any cancellation (a), after the first cancellation (b), and after the last cancellation (c).

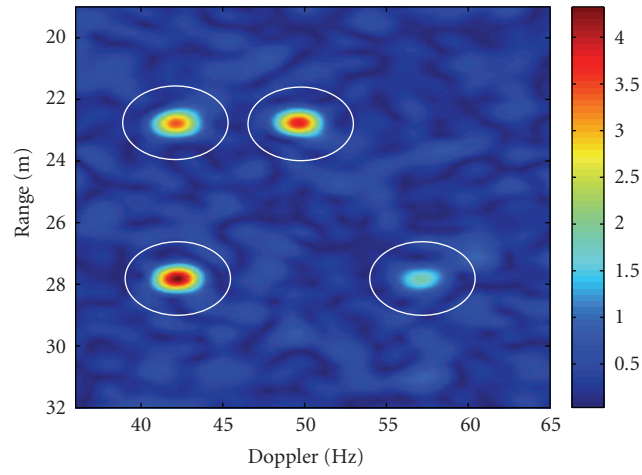

(a)

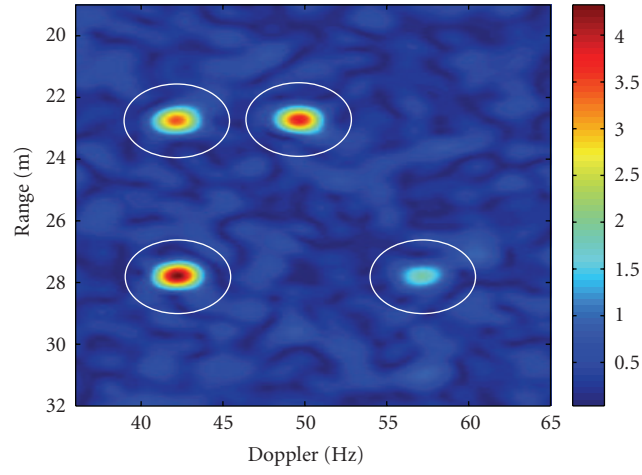

(b)

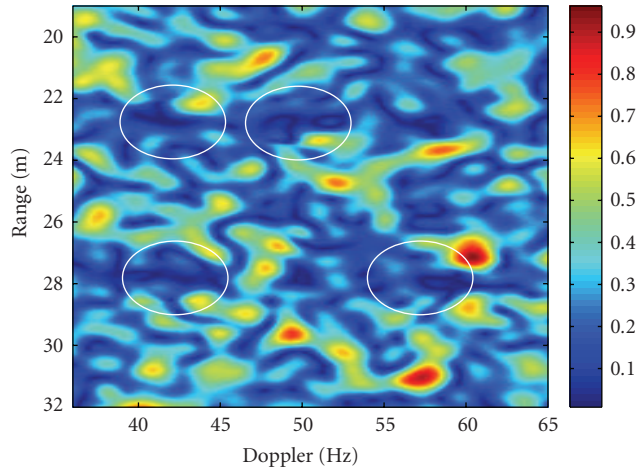

(c)

Figure 6: ISAR image on channel VV-HH before any cancellation (a), after the first cancellation (b), and after the last cancellation (c).

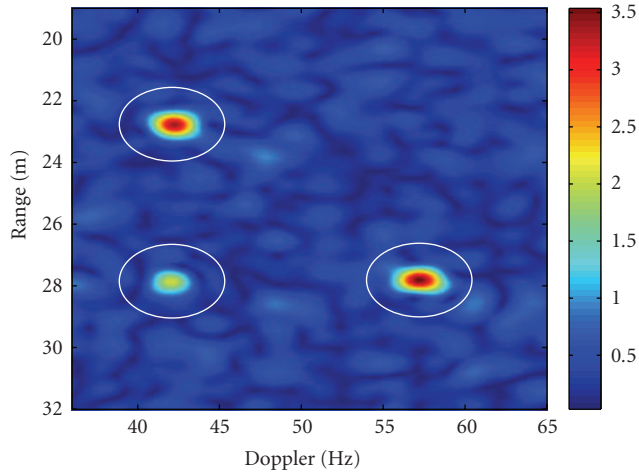

(a)

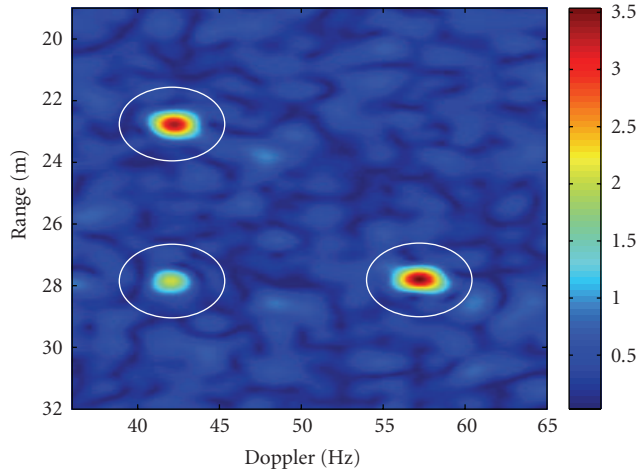

(b)

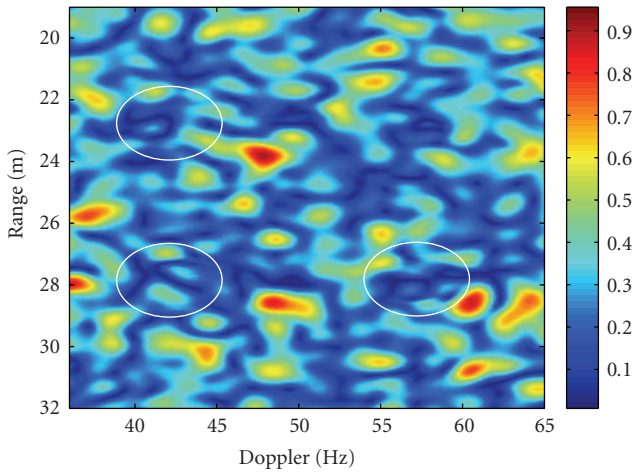

(c)

Figure 7: ISAR image on channel HV before any cancellation (a), after the first cancellation (b), and after the last cancellation (c).

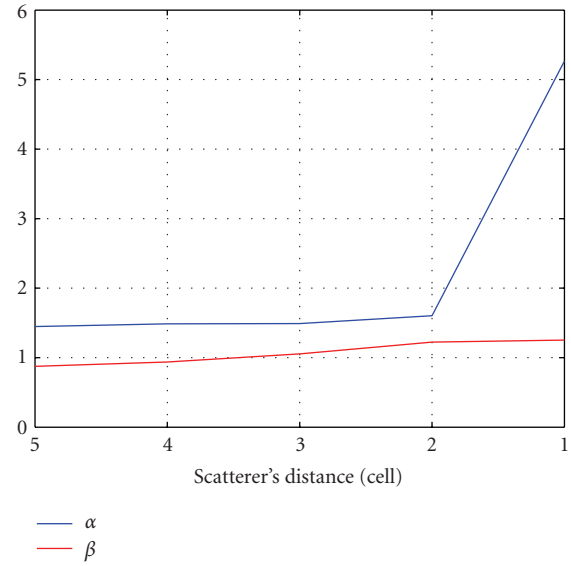

Figure 8: RMSE against the distance in range.

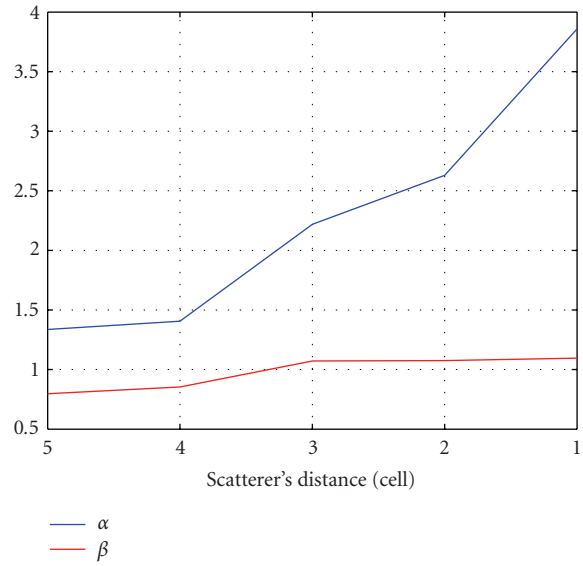

Figure 9: RMSE against the distance in cross range.

the central azimuth angle ($\theta_{az} = 89.231°$). The central frequency is equal to $f_0 = 9.6$ GHz whereas the number of transmitted frequencies is equal to 221, equally spaced by 3 MHz. The resultant bandwidth is equal to 660 MHz and both the nominal range and cross-range resolutions are equal to 0.3048 m.

The radar-target geometry is depicted in Figure 10, whereas the target is shown in Figure 11. The radar parameters are shown in Table 4.

4.2.2. Real data results

The image cross-range section cut across the scattering centre peak (in blue) and the estimated cross-range section of the

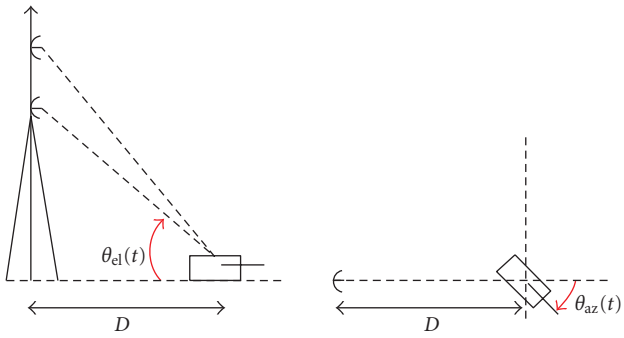

Figure 10: Radar target geometry.

Figure 11: Target T72.

Table 4: Radar parameters.

Parameters	Value
f_0	9.6 Ghz
Frequency step	3 Mhz
N° transmitted frequencies	221
N° sweeps	79
Azimutal sampling rate	0.05°
Total aspect angle for each file	3.9°
Nominal range resolution	1 foot
Nominal cross-range resolution	1 foot

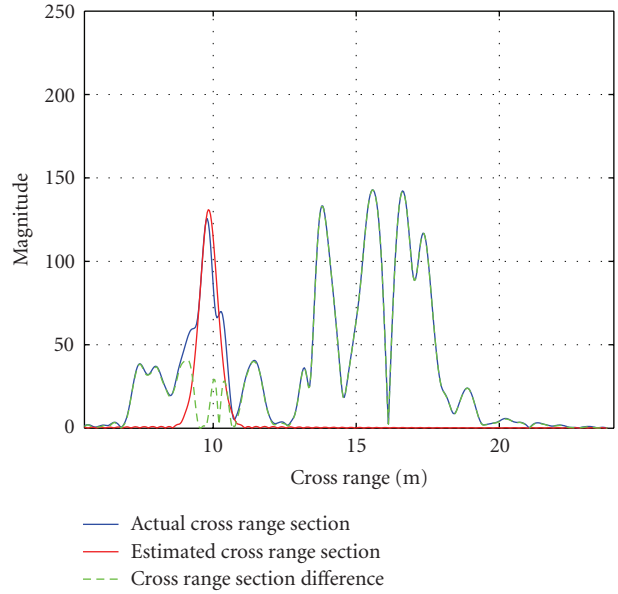

Figure 12: Polarimetric channel HH+VV.

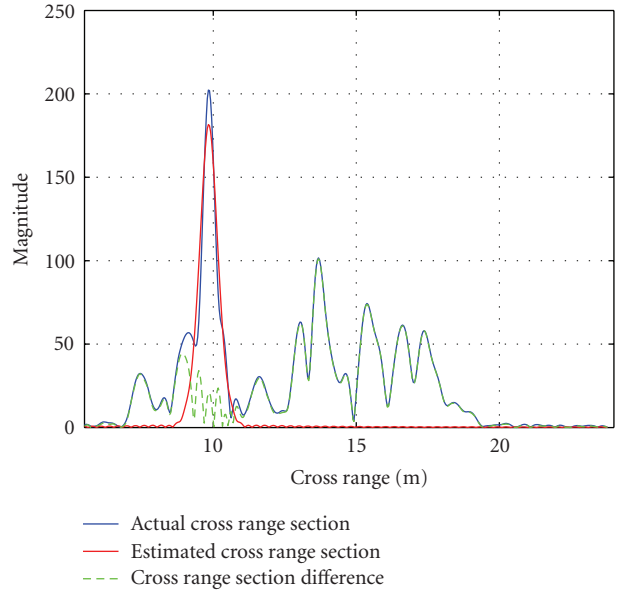

Figure 13: Polarimetric channel VV-HH.

scattering centre PSF (in red) are shown, for all polarimetric channels, in Figures 12, 13, and 14. Moreover, the cross-range section after the scattering centre removal is shown in green colour. It is worth noting that the estimated PSF cross-range section is estimated quite accurately, and therefore the scattering centre is removed from the image. The range section of the same scattering centre, as well as the range section of the estimated PSF, is shown in Figures 15, 16, and 17. It can be noted that the results along the range direction are similar to those along the cross-range direction. Figures 18, 19, 21, 22, 24 and 25 show the ISAR image before and after the cancellation of the first scatterer, for all three polarimetric channel. Figures **??**, 23, 26 how the ISAR images after the cancellation of the last scatterer. By setting the energy threshold defined in (14) to $K = 0.05$, a number of 43 scatterers are extracted. The RGB ISAR image of the target is also shown in Figure 27. The colored dots represent the scattering centres extracted by means of the Pol-CLEAN. The colour of each dot represents the polarimetric signature of the extracted scattering centre in the Pauli basis. It should be noted that the colour of the extracted dot is very close to the colour of the underlying ISAR image, especially in the case of bright scatterers. Weaker extracted scatterers do not match perfectly the colour of the underlying ISAR image. This can be explained by considering that

(1) weaker scatterers are partially masked by stronger scatterer's sidelobes (it can be read as an interference problem);

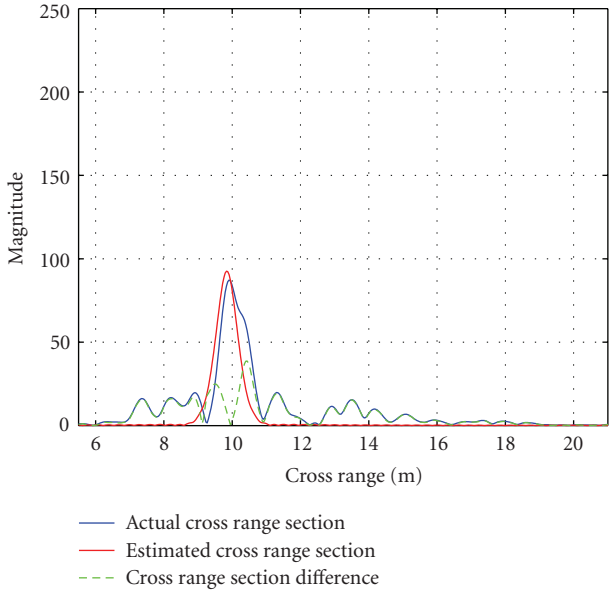

Figure 14: Polarimetric channel 2HV.

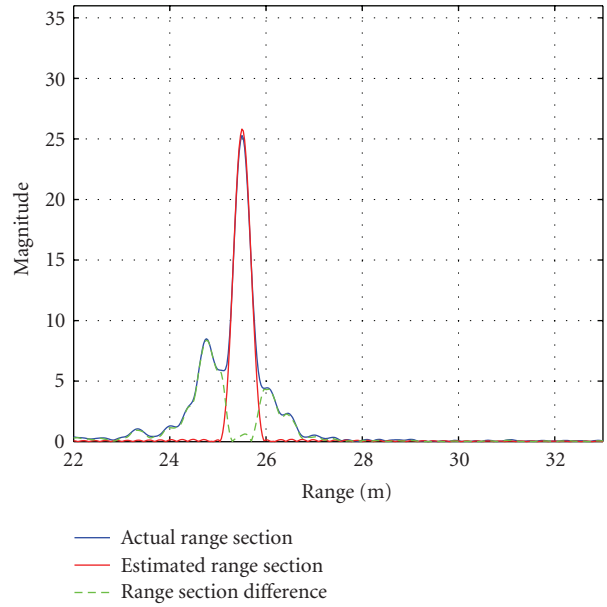

Figure 16: Polarimetric channel VV-HH.

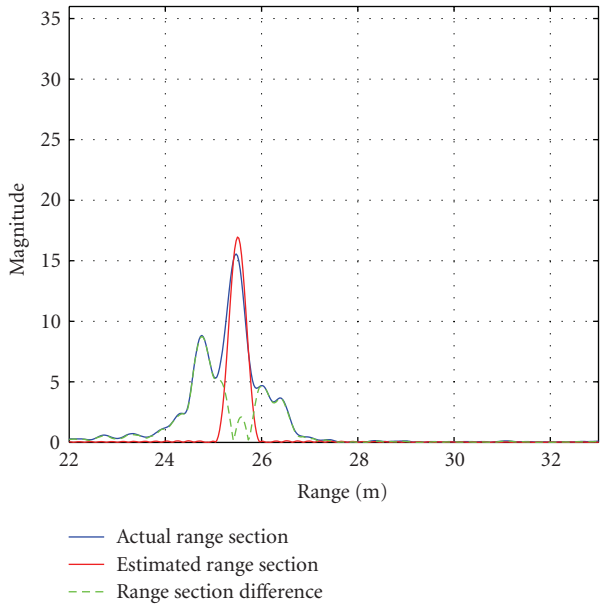

Figure 15: Polarimetric channel HH+VV.

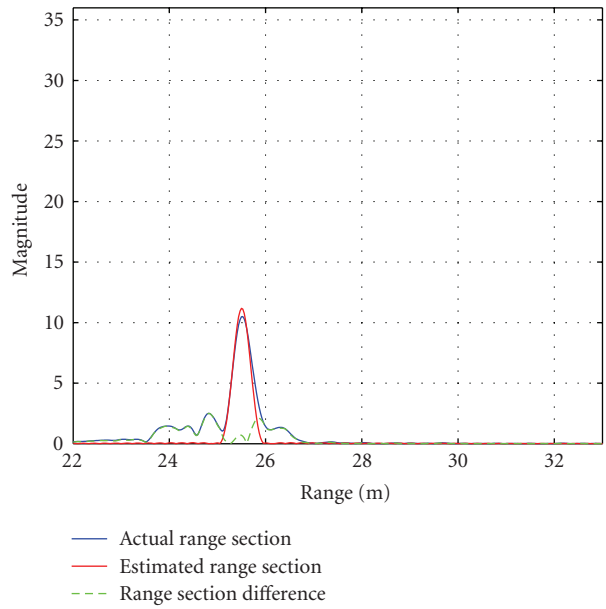

Figure 17: Polarimetric channel 2HV.

(2) even after stronger scatterers are removed, some residuals remain that affect the extraction of weaker scatterers and therefore lead to larger estimation errors.

Nevertheless, classifiers would weight bright scatterers more than weak scatterers and therefore such an effect would not affect the classification performances significantly.

5. CONCLUSIONS

Scattering centre extraction from polarimetric ISAR images can be achieved by extending the CLEAN technique, which was designed to perform scattering centre extraction from single polarization ISAR images. The extension of the CLEAN technique, namely, the Pol-CLEAN technique has been first proposed in this paper and then tested on simulated and real data. The results have shown that the Pol-CLEAN technique is able to extract scattering centres from noisy ISAR images and estimate their locations and polarisation vectors. A table with essential information is then obtained that contains only the positions and polarimetric vectors of the extracted scatterers, which can be used as a feature set for automated target classification and recognition.

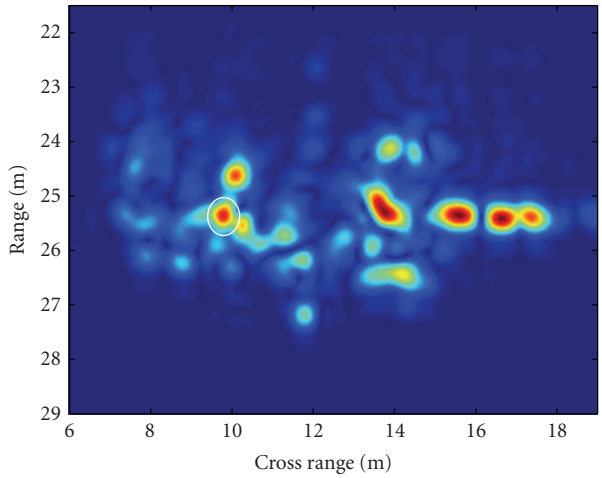

Figure 18: Original ISAR image—polarimetric channel HH+VV.

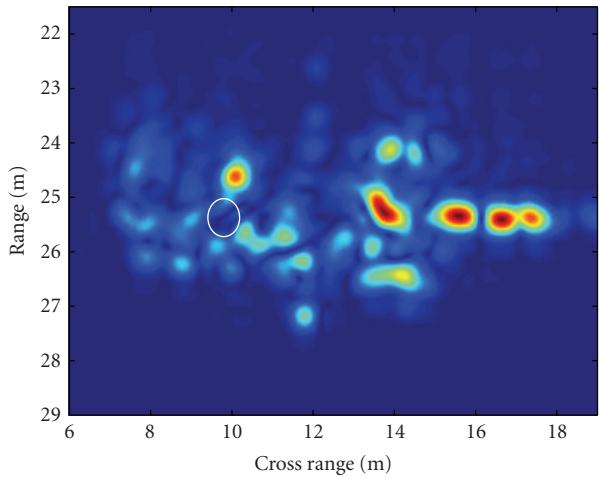

Figure 19: ISAR image after removing the first scattering centre—polarimetric channel HH+VV.

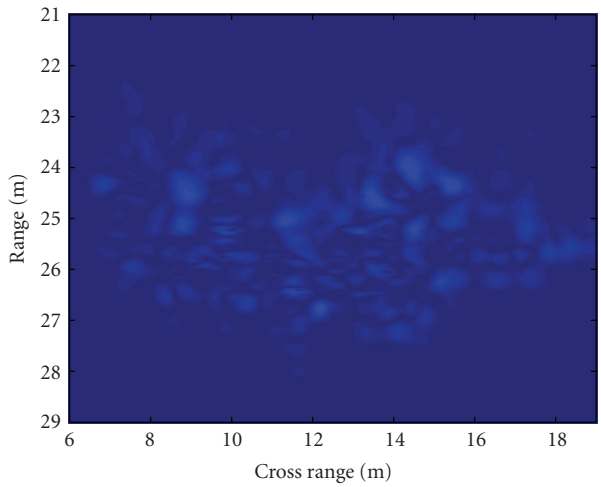

Figure 20: ISAR image after removing the last scattering centre—Polarimetric channel HH+VV.

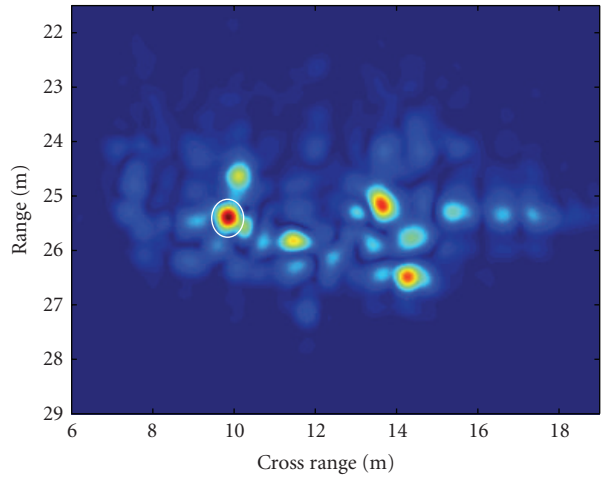

Figure 21: Original ISAR image—polarimetric channel VV-HH.

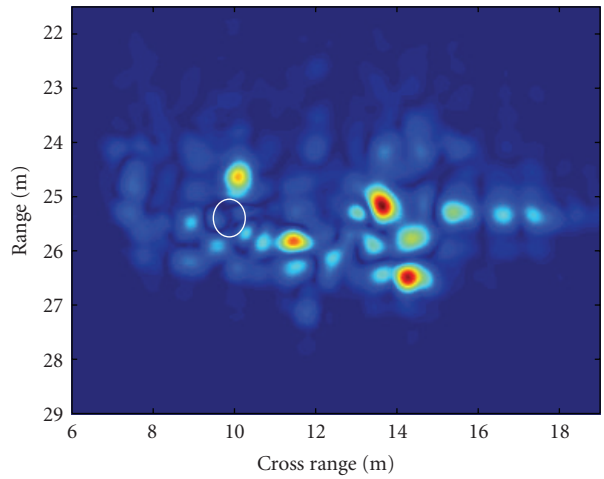

Figure 22: ISAR image after removing the first scattering centre—polarimetric channel VV-HH.

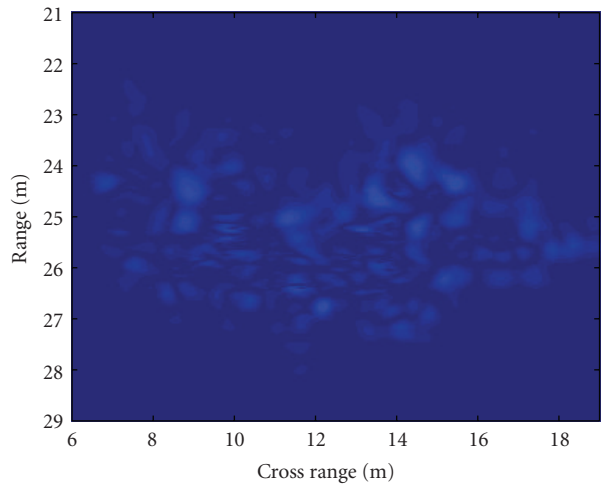

Figure 23: ISAR image after removing the last scattering centre—Polarimetric channel VV-HH.

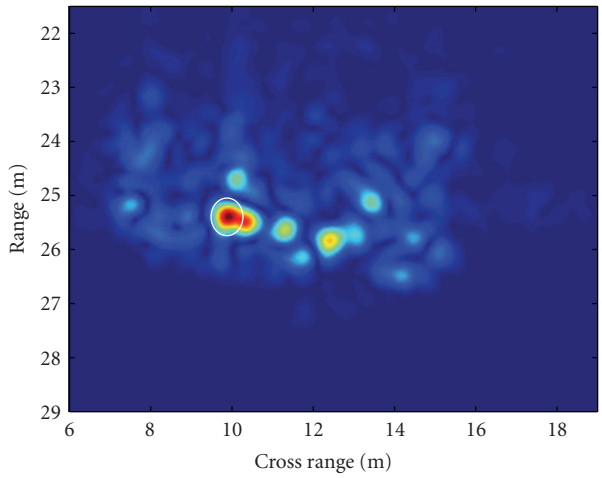

Figure 24: Original ISAR image—Polarimetric channel 2HV.

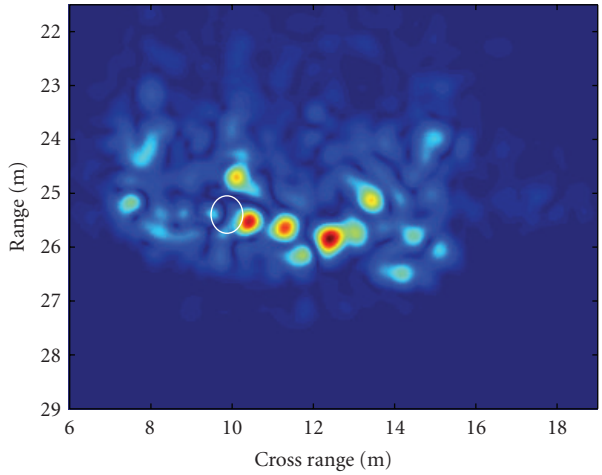

Figure 25: ISAR image after removing the first scattering centre—polarimetric channel 2VH.

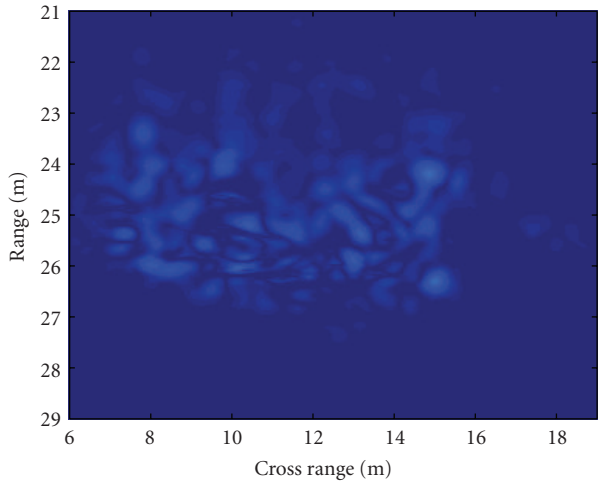

Figure 26: ISAR image after removing the last scattering centre—Polarimetric channel 2HV.

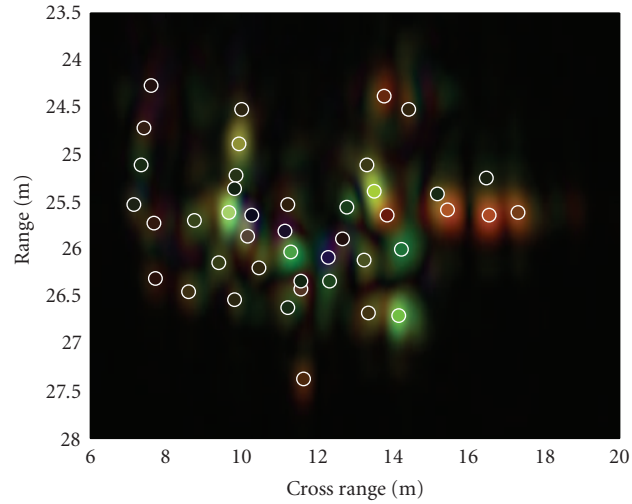

Figure 27: RGB ISAR of the target—the colored spots represent the scatterer extracted by the algorithm.

ACKNOWLEDGMENTS

The authors would like to thank The Sensor ATR Technology Division of the US Air Force Research Laboratory (AFRL) for releasing real data and the Australian Defence Science and Technology Organisation (DSTO) for partially funding this work. The views and conclusions contained in this document are those of the authors and should not be interpreted as representing the official policies, either expressed or implied, of the Defense Advanced Research Projects Agency, the United States Air Force, the Department of Defense, or the US Government.

REFERENCES

[1] J. Tsao and B. D. Steinberg, "Reduction of sidelobe and speckle artifacts in microwave imaging: the CLEAN technique," *IEEE Transactions on Antennas and Propagation*, vol. 36, no. 4, pp. 543–556, 1988.

[2] Y. Sun and P. Lin, "An improved method of ISAR image processing," in *Proceedings of the 35th Midwest Symposium on Circuits and System*, vol. 2, pp. 983–986, Washington, DC, USA, August 1992.

[3] S. R. Cloude and K. P. Papathanassiou, "Polarimetric SAR interferometry," *IEEE Transactions on Geoscience and Remote Sensing*, vol. 36, no. 5, part 1, pp. 1551–1565, 1998.

[4] R. Touzi and F. Charbonneau, "Characterization of target symmetric scattering using polarimetric SARs," *IEEE Transactions on Geoscience and Remote Sensing*, vol. 40, no. 11, pp. 2507–2516, 2002.

[5] M. Martorella, J. Palmer, B. D. Bates, F. Berizzi, and B. Haywood, "Polarimetric hot spot processing for ISAR image autofocusing," in *Proceedings of the IET International Conference on Radar Systems (RADAR '07)*, Edimburgh, UK, October 2007.

[6] W. L. Cameron, N. N. Youssef, and L. K. Leung, "Simulated polarimetric signatures of primitive geometrical shapes," *IEEE Transactions on Geoscience and Remote Sensing*, vol. 34, no. 3, pp. 793–803, 1996.

[7] S. R. Cloude and E. Pottier, "A review of target decomposition theorems in radar polarimetry," *IEEE Transactions on Geoscience and Remote Sensing*, vol. 34, no. 2, pp. 498–518, 1996.
[8] J. R. Huynen, "Measurement of the target scattering matrix," *Proceedings of IEEE*, vol. 53, no. 8, pp. 936–946, 1965.
[9] E. Krogager, "New decomposition of the radar target scattering matrix," *Electronics Letters*, vol. 26, no. 18, pp. 1525–1527, 1990.
[10] T. Cooke, M. Martorella, B. Haywood, and D. Gibbins, "Use of 3D ship scatterer models from ISAR image sequences for target recognition," *Digital Signal Processing*, vol. 16, no. 5, pp. 523–532, 2006.
[11] K.-T. Kim, D.-K. Seo, and H.-T. Kim, "Efficient classification of ISAR images," *IEEE Transactions on Antennas and Propagation*, vol. 53, no. 5, pp. 1611–1621, 2005.
[12] L. Vignaud, "Robust polarimetric scatterers extraction for SAR ATR," in *Proceedings of the RTO-SET Symposium on Target Identification and Recognition Using RF Systems*, Oslo, Norway, October 2004.
[13] M. Martorella, F. Berizzi, and B. Haywood, "Contrast maximisation based technique for 2-D ISAR autofocusing," *IEE Proceedings: Radar, Sonar and Navigation*, vol. 152, no. 4, pp. 253–262, 2005.